LETTER

doi:10.1038/nature16155

Quantum superposition at the half-metre scale

T. Kovachy[1], P. Asenbaum[1], C. Overstreet[1], C. A. Donnelly[1], S. M. Dickerson[1], A. Sugarbaker[1], J. M. Hogan[1] & M. A. Kasevich[1]

The quantum superposition principle allows massive particles to be delocalized over distant positions. Though quantum mechanics has proved adept at describing the microscopic world, quantum superposition runs counter to intuitive conceptions of reality and locality when extended to the macroscopic scale[1], as exemplified by the thought experiment of Schrödinger's cat[2]. Matter-wave interferometers[3], which split and recombine wave packets in order to observe interference, provide a way to probe the superposition principle on macroscopic scales[4] and explore the transition to classical physics[5]. In such experiments, large wave-packet separation is impeded by the need for long interaction times and large momentum beam splitters, which cause susceptibility to dephasing and decoherence[1]. Here we use light-pulse atom interferometry[6,7] to realize quantum interference with wave packets separated by up to 54 centimetres on a timescale of 1 second. These results push quantum superposition into a new macroscopic regime, demonstrating that quantum superposition remains possible at the distances and timescales of everyday life. The sub-nanokelvin temperatures of the atoms and a compensation of transverse optical forces enable a large separation while maintaining an interference contrast of 28 per cent. In addition to testing the superposition principle in a new regime, large quantum superposition states are vital to exploring gravity with atom interferometers in greater detail. We anticipate that these states could be used to increase sensitivity in tests of the equivalence principle[8–12], measure the gravitational Aharonov–Bohm effect[13], and eventually detect gravitational waves[14] and phase shifts associated with general relativity[12].

Progress in the ability to manipulate quantum systems has enabled experimental tests of the foundations of quantum mechanics. These include studies of entanglement[15], tests of local realism with Bell experiments[16,17], and exploration of wave–particle duality in delayed choice experiments with photons[18] and atoms[19]. The quantum superposition principle is a central axiom of quantum mechanics, and efforts to test its universal validity have attracted much interest[1]. A breakdown of quantum superposition at large scales could arise from fundamental modifications to quantum dynamics[4,5], interaction with a field of cosmological origin[5], or quantum gravitational effects[1,5]. Currently, the best bounds on such decoherence mechanisms at large length scales come from matter-wave interference experiments[1,4]. No violations of the quantum superposition principle have yet been detected. To bound or discover such violations at macroscopic scales requires a well-controlled system that limits dephasing and decoherence from conventional and technical sources.

Atom interferometry offers a way to create and characterize atomic superpositions. The field of atom interferometry has developed as a long series of experiments originating from Bordé's realization of the importance of recoil effects in precision Ramsey laser spectroscopy[6,20], which led to the Bordé–Ramsey technique[6,20]. Other important developments include the demonstration of atom interferometers using mechanical gratings[21] and two-photon transitions[7].

To create large atomic quantum superpositions, a significant challenge is to combine large momentum transfer (LMT) atomic beam splitters[22,23] with long-time (>2 s) atom interferometry[24,25]. Interferometers with LMT beam splitters are susceptible to dephasing from laser intensity inhomogeneity and wavefront perturbations across the atom cloud. These dephasing mechanisms are coupled to the transverse expansion of the atom cloud and are therefore exacerbated by long interferometer durations.

We achieve long free-fall times by launching a Bose–Einstein condensed cloud of $\sim 10^5$ ultracold ^{87}Rb atoms into a 10 m atomic fountain using a chirped optical lattice[24]. After the lattice launch, we use a sequence of optical pulses to apply a beam splitter that places each atom into a superposition of two wave packets with different momenta, corresponding to the two arms of a Mach–Zehnder interferometer[7]. We then allow the two wave packets to spatially separate vertically during a drift time $T = 1.04$ s. Subsequently, we redirect the two wave packets back towards each other with additional optical pulses (the mirror sequence), and cause them to interfere using a final beam splitter when they once again spatially overlap after another drift interval of $T = 1.04$ s. Finally, we image the two interferometer output ports using a CCD camera (see Fig. 1).

The maximum spatial separation reached in the interferometer is $\Delta z = n(\hbar k/m)T$, where k is the laser wave number, n is the number of photon recoils ($\hbar k$) transferred by the beam splitter, and m is the atomic mass ($\hbar k/m$ is the velocity associated with a single photon momentum recoil). Our LMT beam splitters transfer up to $90\hbar k$, yielding superpositions with much larger spatial separation than is possible with conventional $2\hbar k$ atom optics (54 cm for $90\hbar k$, as shown in Fig. 2). We realize the beam splitters with sequential $2\hbar k$ Bragg transitions[23] (see Methods). The laser beams that drive the Bragg transitions are sent into the atomic fountain from the top and retroreflected by a mirror at the bottom.

To quantify the coherence of the macroscopic superposition states, we measure the contrast of the interferometer. To determine the contrast, we record the amount of variation in the normalized population in one of the output ports as it varies between constructive and destructive interference. The normalized population in output port i is $P_i \equiv N_i/(N_1 + N_2)$, where N_i is the measured atom number in output port i. Owing to interference between the two arms of the interferometer, the population oscillates between the two output ports[24]. Examples of fluorescence images showing this population modulation are given in Fig. 3.

Owing to the large enclosed space-time area ΔzT, the interferometer is highly sensitive to acceleration. Specifically, the sensitivity of the interferometer phase ϕ to an acceleration a can be expressed as[7] $\Delta\phi = ma\Delta zT/\hbar$. This leads to an acceleration response for our interferometer of 2×10^8 rad per g for $2\hbar k$ beam splitters and 8×10^9 rad per g for $90\hbar k$ beam splitters (g is the acceleration due to gravity). Consequently, the interferometer phase fluctuates by much more than 2π from shot to shot due to vibration of the retroreflection mirror, causing the output ports to vary randomly between constructive and destructive interference. Therefore, we see significant contrast, but the large acceleration sensitivity prevents the observation of a stable fringe as the phase is scanned. Since the contrast quantifies the coherence of the macroscopic superposition states, the contrast is the relevant metric for this work (as in photon recoil measurements with contrast

[1]Department of Physics, Stanford University, Stanford, California 94305, USA.

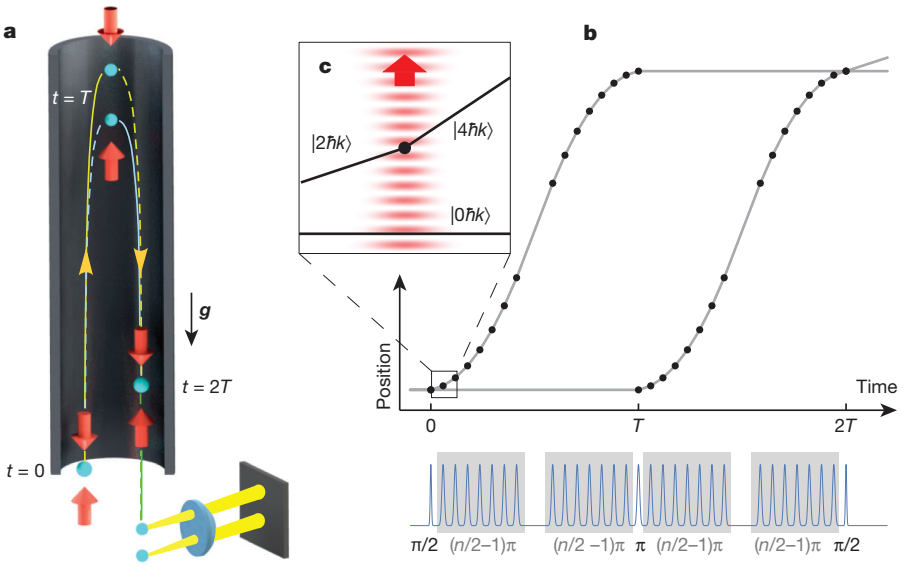

Figure 1 | Fountain interferometer. a, After evaporative cooling and a magnetic lensing sequence (see Methods), the ultra-cold atom cloud is launched vertically from below the cylindrical magnetic shield using an optical lattice. At $t = 0$, the first beam splitter sequence splits the cloud into a superposition of momentum states separated by $n\hbar k$. At $t = T$, the wave packet is fully separated, and a mirror sequence reverses the momentum states of the two halves of the cloud. At $t = 2T$, the clouds spatially overlap, and a final beam splitter sequence is applied. After a short drift time, the output ports spatially separate by 6 mm owing to their differing momenta, and the two complementary ports are imaged. This diagram is not to scale, and the upward- and downward-going clouds are shown horizontally displaced for clarity. The red, cylindrical arrows illustrate the counter-propagating laser beams that drive the Bragg transitions. The blue spheres represent the atomic wave packets. The solid and dashed lines show the trajectories of the atomic wave packets (solid lines correspond to $n\hbar k$ greater momentum in the upward direction than the dashed lines), and the yellow arrowheads indicate the direction of motion. **b**, Pulse sequence of a $16\hbar k$ interferometer, see Methods for details. The main plot depicts the spacetime trajectories of the wave packets, and the pulse train underneath shows the temporal profile of the laser pulse sequences. **c**, A moving standing wave (red wave, direction of motion indicated by red arrow) induces a Bragg transition of one specific velocity class and changes its momentum by $2\hbar k$, for example, from $2\hbar k$ to $4\hbar k$. The black lines show a zoomed-in view of the spacetime trajectories, labelled by momentum. The black dot indicates the point at which the transition from momentum $2\hbar k$ to $4\hbar k$ occurs.

interferometry[26]). In many future experiments to explore gravitational physics, differential measurement schemes[27] (for example, gravity gradiometry) will be used to exploit the increased sensitivity offered by large superposition states while cancelling the vibration-induced phase noise as a common mode[12–14]. In the work presented here, common-mode cancellation of the vibration-induced phase noise between different parts of the atom cloud allows us to observe contrast and additionally to see spatial interference fringes across the atom cloud (see below).

To further demonstrate interference, we measure the contrast envelope, that is, the variation of P_1 as a function of a timing delay δT before the final beam-recombining pulse sequence. At suitably large delays, contrast is suppressed, thus allowing characterization of technical noise sources which might be conflated with contrast at shorter delays. The timing asymmetry leads to a phase shift $nkv_z\delta T$ that depends on the vertical velocity v_z (refs 24, 25). Integrating over the vertical velocity distribution of the atom cloud after the interferometer (r.m.s. width Δv_z), the contrast is expected to decay with δT as the envelope function[28] $\Gamma(\delta T) \equiv \exp[-n^2k^2\Delta v_z^2\delta T^2/2] = \exp[-\delta T^2/2\delta T_c^2]$, where the coherence time is given by $\delta T_c \equiv 1/(nk\Delta v_z)$. Figure 4a displays the contrast envelopes and comparison to theory for $30\hbar k$, $60\hbar k$, and $90\hbar k$ beam splitters. We plot $\sigma(P_1)$, the standard deviation of the set of observed P_1 values after a sequence of 20 shots at the specified δT, as δT is varied (see also Extended Data Fig. 2). Note that $2\sqrt{2}\,\sigma(P_1)$ is approximately equal to the contrast[22]. The data closely match the expected decay dependence $\Gamma(\delta T)$ for the known values of n, k and Δv_z.

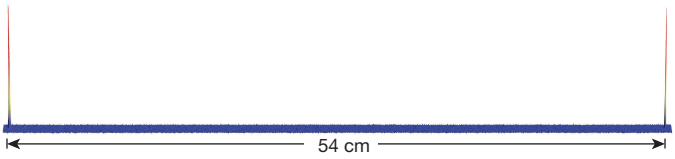

Figure 2 | Wave packets separated by 54 cm. We adjust the launch height of the millimetre-sized atom cloud so that it passes the detector when the wave packets (corresponding to the two peaks in the image) are maximally separated. In order to visualize the full extent of the wave function, we take 36 snapshots of different slices of the distribution. The images are taken at slightly different times between the atom launch and the fluorescence imaging and are stitched together according to the velocity of the atoms. The vertical height in the plot corresponds to atom density (red indicates higher density).

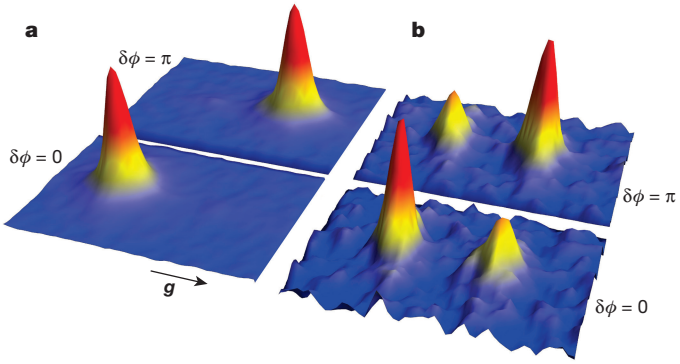

Figure 3 | Fluorescence images of output ports. The two atom clouds resulting from the final beam splitter constitute the output ports of the interferometer. A single fluorescence image allows us to extract the atom number in each port. **a**, The $2\hbar k$ interferometer shows high contrast with nearly full population oscillation between the upper port (front image) and the lower port (back image). **b**, For the $90\hbar k$ interferometer, the population oscillates by more than 40%. Owing to spontaneous emission and velocity selectivity, the detected atom number is more than ten times smaller than for $2\hbar k$. All displayed images are normalized to have the same peak height and are labelled with $\delta\phi$ corresponding to the interferometer phase modulo 2π. Each image is 13.8×9.7 mm, and the data are smoothed with a Gaussian filter with radius 0.5 mm.

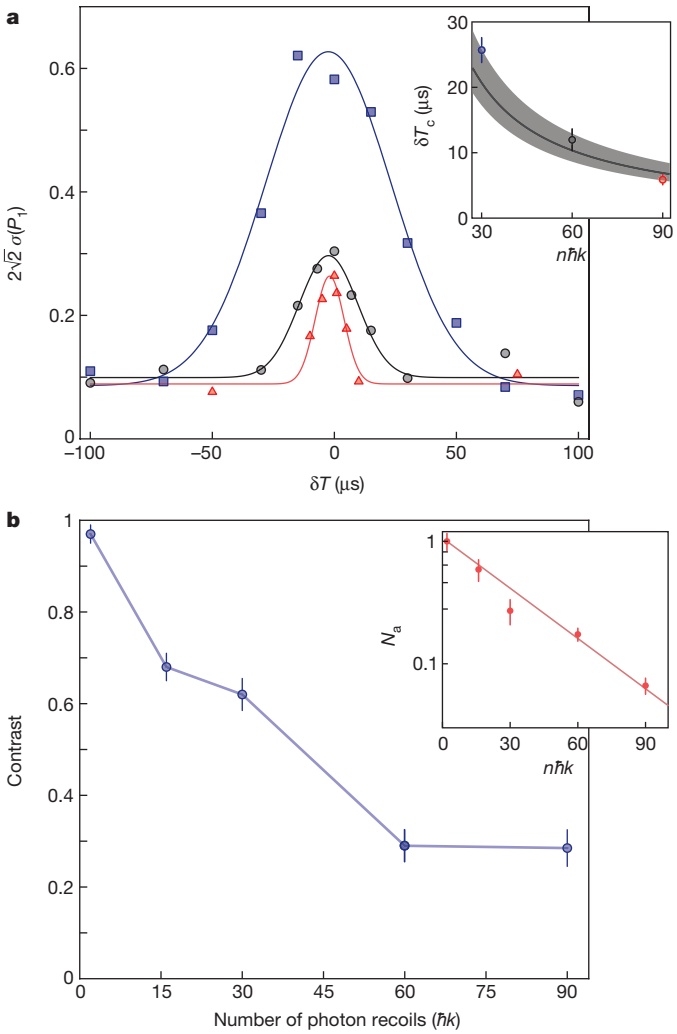

Figure 4 | Contrast metrics. a, The contrast envelopes establish the interference effect. We plot $2\sqrt{2}\,\sigma(P_1)$ versus the timing delay δT, where $\sigma(P_1)$ is the standard deviation of the set of observed P_1 values after a sequence of 20 shots at the specified δT (P_1 is the normalized population in output port 1). The data points corresponding to the blue squares, black circles and red triangles are for $30\hbar k$, $60\hbar k$ and $90\hbar k$. The solid curves show the theory $A + BI(\delta T - \delta T_0)$, with coherence time δT_c, offset A, centre δT_0, and amplitude B as fitting parameters. Examples of the traces that lead to the points in the contrast envelopes are shown in Extended Data Fig. 2. Inset, comparison of fitted coherence times (points, 1 s.d. error bars from fit uncertainty) to theory (grey curve). The grey, shaded region indicates 1 s.d. theoretical uncertainty arising from uncertainty in the measured velocity spread Δv_z. **b**, Trends in maximum observed contrast (blue data points, main panel) and normalized atom number N_a in the output ports (red data points, inset) with $n\hbar k$. The data points are for $n = 2$, 16, 30, 60 and 90. The atom number is normalized to the average number of atoms after a $2\hbar k$ interferometer. The thin, red curve in the inset shows the predicted atom number based on the measured spontaneous emission loss rate and π-pulse velocity selectivity. Error bars, 1 s.d. uncertainties computed with the analysis discussed in Methods.

Given that the atom cloud has a known time $t_e = 2.6$ s to expand, the vertical size of the interferometer output ports provides us with an independent measurement of $\Delta v_z = 0.20 \pm 0.04\,\mathrm{mm\,s^{-1}}$. The measured coherence times, as determined by fits of the contrast envelope widths, show quantitative agreement with their theoretically predicted values (see Fig. 4a).

Figure 4b shows the interference contrast for various values of n. To determine the contrast value for a given n, we use maximum likelihood estimation on the data corresponding to the highest point in the contrast envelope (see Methods). The model used to estimate the contrast

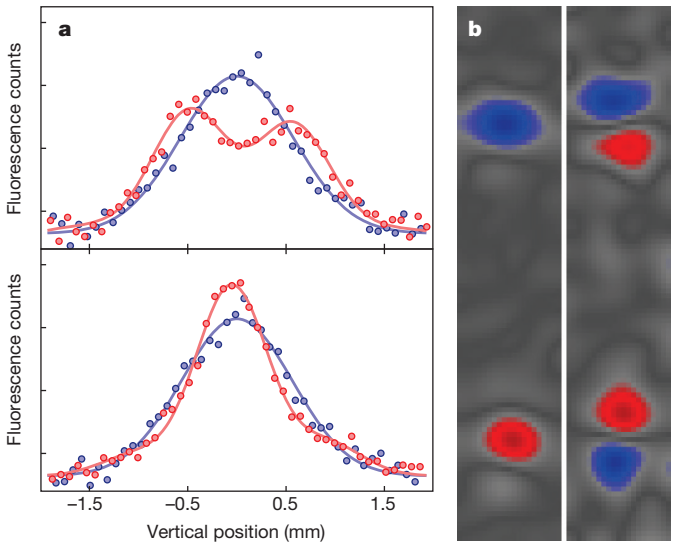

Figure 5 | Spatial interference fringes. a, Horizontally integrated fluorescence images of the two $30\hbar k$ output ports (upper and lower panel) for a single run with $\delta T = -50$ μs (red). The images are fitted to a sinusoidally modulated Gaussian profile. For comparison, the output ports for $\delta T = 100$ μs have a Gaussian profile without interference fringes (blue). y axis in arbitrary units. **b**, Cosine (left panel) and sine (right panel) principal components of a set of $30\hbar k$ interferometer runs with $\delta T = -50$ μs, which show the effects of a vertical phase gradient across the cloud. All observed fringes are linear combinations of these basis images. Red and blue regions are anti-correlated.

corrects for the technical noise measured away from the contrast peak (that is, at large δT). Also, Fig. 4b inset shows the exponential scaling of atom loss with n. Atom loss derives from two factors: spontaneous emission decay with $1/e$ point $n = 75 \pm 10$, and residual velocity selection of the π-pulses.

A complementary demonstration of interference is the observation of spatial interference fringes across the atom cloud for small timing delays δT (refs 25,29). The predicted fringe wavelength is $\lambda_z = 2\pi t_e/(nk|\delta T - \delta T_0|)$, where t_e is the cloud expansion time and δT_0 accounts for velocity-dependent phase shifts from force gradients[29] (see Methods). Figure 5a shows an unsmoothed example of the directly observed fringe from a single shot. The 1σ uncertainty in the phase extracted from fitting the fringe is 0.1 rad, which is near the atom shot noise limit for the observed contrast. For $\delta T = -50$ μs the fitted wavelength $\lambda_z = 1.5 \pm 0.1$ mm (1σ error from fit uncertainty) agrees with the theoretical value of $\lambda_z = 1.4$ mm (taking $\delta T_0 = 0$). Assuming a spherical Earth's gravity gradient would shift the prediction to $\lambda_z = 1.5$ mm. This is equivalent to $\delta T_0 = -3.5$ μs, which is likely to be the reason why δT_0 is slightly negative for the contrast envelopes in Fig. 4a. While the overall position of the spatial fringes varies from shot to shot, the fringes on the two ports always have complementary phases, as expected. Using principal component analysis on a set of 20 images, we extract the two orthogonal modes describing the spatial fringe[24] (Fig. 5b).

Even for the 54 cm delocalization and a total of 180 applied optical Bragg pulses, we observe a contrast of 28%. We attribute the ability to maintain this level of contrast to two factors: the low temperature of the atoms and an absolute light shift compensation technique (see Methods). The ultra-cold cloud remains smaller than 1 mm throughout the interferometer. This reduces the contrast loss due to larger-scale inhomogeneities in laser intensity and wavefront (for example, from the 2 cm laser radial waist). The small cloud also minimizes pollution of the output ports by non-interfering atoms originating from spontaneous emission and imperfect transfer efficiency. The importance of absolute light shift compensation is demonstrated by the fact that operating without compensation almost fully eliminates the contrast for a $30\hbar k$ interferometer (see Extended Data Fig. 1). Further improvement of the contrast at large $n\hbar k$ is likely to require reduction of wavefront

perturbations, since these are intrinsically imprinted on the cloud at each pulse.

We probe the quantum superposition principle in an unprecedented regime. Extended Data Table 1 compares the wave-packet separation, interferometer duration, and mass of our superposition states to those of other matter-wave interferometers, showing that we occupy a new region of large wave-packet separation and long time. As a result, we set new bounds on macroscopic extensions of quantum mechanics (see Extended Data Fig. 3 and Methods) that introduce a decoherence mechanism for superpositions larger than a certain critical size (the critical size is a free parameter of the theory)[4]. For instance, as shown in Extended Data Fig. 3, our bound on the decoherence rate for critical sizes $\gtrsim$1 m is 10^4 times stronger than those placed by other experiments. In addition, these large superposition states pave the way for a new generation of fundamental physics tests using ultrasensitive atom interferometers[12–14]. The wave-packet delocalization and coherence time demonstrated here already meet the requirements for certain proposed atomic gravitational wave detectors[14]. The demonstrated enclosed space-time area combined with optical atomic clock states could also enable the study of decoherence induced by general relativistic proper time[30].

Online Content Methods, along with any additional Extended Data display items and Source Data, are available in the online version of the paper; references unique to these sections appear only in the online paper.

Received 19 June; accepted 9 October 2015.

1. Arndt, M. & Hornberger, K. Testing the limits of quantum mechanical superpositions. *Nature Phys.* **10,** 271–277 (2014).
2. Schrödinger, E. Die gegenwärtige Situation in der Quantenmechanik. *Naturwissenschaften* **23,** 807–812 (1935).
3. Cronin, A. D., Schmiedmayer, J. & Pritchard, D. E. Optics and interferometry with atoms and molecules. *Rev. Mod. Phys.* **81,** 1051–1129 (2009).
4. Nimmrichter, S. & Hornberger, K. Macroscopicity of mechanical quantum superposition states. *Phys. Rev. Lett.* **110,** 160403 (2013).
5. Bassi, A., Lochan, K., Satin, S., Singh, T. & Ulbricht, H. Models of wave-function collapse, underlying theories, and experimental tests. *Rev. Mod. Phys.* **85,** 471–527 (2013).
6. Bordé, C. J. Atomic interferometry with internal state labelling. *Phys. Lett. A* **140,** 10–12 (1989).
7. Kasevich, M. & Chu, S. Atomic interferometry using stimulated Raman transitions. *Phys. Rev. Lett.* **67,** 181–184 (1991).
8. Bonnin, A., Zahzam, N., Bidel, Y. & Bresson, A. Simultaneous dual-species matter-wave accelerometer. *Phys. Rev. A* **88,** 043615 (2013).
9. Schlippert, D. *et al.* Quantum test of the universality of free fall. *Phys. Rev. Lett.* **112,** 203002 (2014).
10. Kuhn, C. C. N. *et al.* A Bose-condensed, simultaneous dual-species Mach-Zehnder atom interferometer. *New J. Phys.* **16,** 073035 (2014).
11. Geiger, R. *et al.* Detecting inertial effects with airborne matter-wave interferometry. *Nature Commun.* **2,** 474 (2011).
12. Dimopoulos, S., Graham, P., Hogan, J. & Kasevich, M. General relativistic effects in atom interferometry. *Phys. Rev. D* **78,** 042003 (2008).
13. Hohensee, M. A., Estey, B., Hamilton, P., Zeilinger, A. & Müller, H. Force-free gravitational redshift: proposed gravitational Aharonov-Bohm experiment. *Phys. Rev. Lett.* **108,** 230404 (2012).
14. Dimopoulos, S., Graham, P., Hogan, J., Kasevich, M. & Rajendran, S. Atomic gravitational wave interferometric sensor. *Phys. Rev. D* **78,** 122002 (2008).
15. Julsgaard, B., Kozhekin, A. & Polzik, E. S. Experimental long-lived entanglement of two macroscopic objects. *Nature* **413,** 400–403 (2001).
16. Aspect, A., Dalibard, J. & Roger, G. Experimental test of Bell's inequalities using time-varying analyzers. *Phys. Rev. Lett.* **49,** 1804–1807 (1982).
17. Giustina, M. *et al.* Bell violation using entangled photons without the fair-sampling assumption. *Nature* **497,** 227–230 (2013).
18. Jacques, V. *et al.* Experimental realization of Wheeler's delayed-choice gedanken experiment. *Science* **315,** 966–968 (2007).
19. Manning, A. G., Khakimov, R. I., Dall, R. G. & Truscott, A. G. Wheeler's delayed-choice gedanken experiment with a single atom. *Nature Phys.* **11,** 539–542 (2015).
20. Bordé, C. J. *et al.* Observation of optical Ramsey fringes in the 10 μm spectral region using a supersonic beam of SF_6. *J. Phys. (Paris)* **42**(C8), 15–19 (1981).
21. Keith, D. W., Ekstrom, C. R., Turchette, Q. A. & Pritchard, D. E. An interferometer for atoms. *Phys. Rev. Lett.* **66,** 2693–2696 (1991).
22. Müller, H., Chiow, S.-W., Long, Q., Herrmann, S. & Chu, S. Atom interferometry with up to 24-photon-momentum-transfer beam splitters. *Phys. Rev. Lett.* **100,** 180405 (2008).
23. Chiow, S.-W., Kovachy, T., Chien, H.-C. & Kasevich, M. A. 102$\hbar k$ large area atom interferometers. *Phys. Rev. Lett.* **107,** 130403 (2011).
24. Dickerson, S. M., Hogan, J. M., Sugarbaker, A., Johnson, D. M. S. & Kasevich, M. A. Multiaxis inertial sensing with long-time point source atom interferometry. *Phys. Rev. Lett.* **111,** 083001 (2013).
25. Müntinga, H. *et al.* Interferometry with Bose-Einstein condensates in microgravity. *Phys. Rev. Lett.* **110,** 093602 (2013).
26. Gupta, S., Dieckmann, K., Hadzibabic, Z. & Pritchard, D. E. Contrast interferometry using Bose-Einstein condensates to measure h/m and α. *Phys. Rev. Lett.* **89,** 140401 (2002).
27. Foster, G. T., Fixler, J. B., McGuirk, J. M. & Kasevich, M. A. Method of phase extraction between coupled atom interferometers using ellipse-specific fitting. *Opt. Lett.* **27,** 951–953 (2002).
28. Parazzoli, L. P., Hankin, A. M. & Biedermann, G. W. Observation of free-space single-atom matter wave interference. *Phys. Rev. Lett.* **109,** 230401 (2012).
29. Sugarbaker, A., Dickerson, S. M., Hogan, J. M., Johnson, D. M. S. & Kasevich, M. A. Enhanced atom interferometer readout through the application of phase shear. *Phys. Rev. Lett.* **111,** 113002 (2013).
30. Zych, M., Costa, F., Pikovski, I. & Brukner, C. Quantum interferometric visibility as a witness of general relativistic proper time. *Nature Commun.* **2,** 505 (2011).

Acknowledgements We thank S.-w. Chiow for discussions and contributions to the apparatus. T.K. acknowledges support from the Fannie and John Hertz Foundation, T.K. and C.A.D. from the NSF GRFP, and T.K. and C.O. from the Stanford Graduate Fellowship. This work was supported in part by NASA GSFC grant no. NNX11AM31A.

Author Contributions T.K., P.A., C.O., C.A.D., J.M.H. and M.A.K. carried out the experiment, analysed the data and prepared the manuscript. S.M.D. and A.S. contributed significantly to the early stages of the experiment.

Author Information Reprints and permissions information is available at www.nature.com/reprints. The authors declare no competing financial interests. Readers are welcome to comment on the online version of the paper. Correspondence and requests for materials should be addressed to M.A.K. (kasevich@stanford.edu).

METHODS

Atom source. A 2D magneto optical trap (MOT) loads a 3D MOT in the centre of our 10 m vacuum tube for 4 s. We evaporate the ^{87}Rb atoms in a time-orbiting potential (TOP) trap for 14 s and apply a magnetic lensing sequence to further reduce their kinetic energy[31]. The ultra-cold atoms are then launched upwards into the interferometer region with a chirped optical lattice. Overall, we have a cycle time of roughly 22 s.

Atom optics. For the initial beam splitter, a $\pi/2$-pulse splits the interferometer arms in momentum space by $2\hbar k$, followed by a sequence of $(n/2)-1$ π-pulses that selectively accelerate one of the arms to increase the momentum splitting to $n\hbar k$. The mirror sequence consists of $n-1$ sequential π-pulses that interchange the momenta of the two interferometer arms[23,32], and the final beam splitter sequence once again contains $(n/2)-1$ π-pulses applied to one arm followed by a $\pi/2$-pulse.

Bragg transitions couple different momentum states of the hyperfine level $F=2$, $m_F=0$. In contrast to Raman transitions[7,33], a Bragg scheme does not suffer from light-shift-induced variations of the hyperfine splitting between $F=1$ and $F=2$. The optical pulses that drive the Bragg transitions have Gaussian temporal profiles with full-width at half-maximum (FWHM) 60 μs for π-pulses and 30 μs for $\pi/2$-pulses. Before the first beam splitter, the vertical velocity width is filtered by a 300 μs π-pulse that transfers only a narrow velocity slice. The two atom optics laser beams each contain 3 W of power 30 GHz detuned from the excited state resonance and are generated by frequency doubling the outputs of 1,560 nm fibre amplifiers in nonlinear crystals[34]. These beams are combined on a polarizing beam splitter and enter the atomic fountain from the top. They have a radial waist of 2 cm and are retroreflected by a mirror at the bottom of the fountain. The mirror's angle is adjusted between pulse sequences by a piezo-actuated tip-tilt stage to compensate for Coriolis forces from Earth's rotation[24]. Given that the laser intensity is limited by the large beam waist, sequential $2\hbar k$ Bragg transitions offer lower spontaneous emission losses than higher order Bragg transitions[35].

Absolute light shift compensation. We implement a technique to compensate optical dipole forces on the atoms from imperfections in the laser beam profile. Dipole forces arise from gradients in the laser intensity, since the energy of an atomic state is shifted by an amount proportional to the local laser intensity (light shift)[3]. These forces can distort the cloud and cause large differential phase shifts across the cloud. The differential phase shifts occur because the laser intensity profile varies with vertical position and is therefore not fully common to the two interferometer arms. To perform this compensation, we adjust the laser spectrum so that the absolute light shift from the blue-detuned spectral content, including the frequency components that drive the Bragg transitions, is cancelled by the absolute light shift from the red-detuned spectral content.

We achieve a light-shift-compensating spectrum by phase modulating each of the two atom optics lasers at 30 GHz, with the carrier 3.4 GHz blue-detuned from resonance and nearly fully suppressed. The two atom optics lasers are offset by an AOM shift of 160 MHz so that only one pair of sidebands drives Bragg transitions. The phase modulation occurs on the 1,560 nm light seeding the fibre amplifiers. To tune the asymmetry between the red and blue sidebands, we adjust the temperature of the frequency doubling crystals. We measure the optical spectrum with a scanning Fabry–Perot cavity.

Contrast metrics data analysis. Following similar analysis from previous work[11], we model P_1 as a random variable. Our model for the probability density function (PDF) of P_1 includes additive Gaussian noise[11]. P_1 is related to the phase Φ and contrast c of the interferometer by:

$$P_1(\Phi, X; c, w) = \frac{1}{2} + \frac{c}{2}\cos\Phi + X(w) \tag{1}$$

We assume that the interferometer phase is uniformly distributed, so the PDF of Φ is given by $f_\Phi(\phi) = \frac{1}{\pi}$ where $\phi \in [0, \pi]$, and that the amplitude noise X is normally distributed with standard deviation w. We also assume that Φ and X are independent, so the PDF of P_1 in the presence of noise X is equal to the convolution of the PDF of P_1 in the absence of noise ($w \to 0$) with the PDF of X.

Since the contrast approaches zero for large δT, all remaining fluctuations in P_1 at large δT are due to amplitude noise. Therefore, we estimate w by computing the standard deviation of data taken at large values of δT. To estimate c, we use maximum likelihood estimation[36] on the data set corresponding to the highest point in each contrast envelope, taking w to be a fixed parameter. The resulting contrast estimates are plotted in Fig. 4b. To calculate the uncertainty in the contrast estimates, we use the observed Fisher information for each data set[36]. We also propagate the uncertainty in the measured value of w. We discuss this contrast estimation procedure in greater detail below.

Error bars for the atom number in Fig. 4b are computed from statistical standard deviation. The curve showing the predicted atom number in Fig. 4b accounts for atom loss due to spontaneous emission and imperfect π-pulse transfer efficiency. We measure the spontaneous emission loss rate by illuminating the launched cloud with a detuned interferometer pulse sequence. Specifically, all pulses are detuned from their respective two-photon resonances so that there is no transfer. Therefore, the ratio of the number of atoms remaining after such a pulse sequence to the number of atoms remaining after a launch with no pulses allows us to determine the fraction of the atoms lost due to spontaneous emission. To measure the π-pulse transfer efficiency, we apply a $\pi/2$-pulse followed by 44 π-pulses and compare the number of atoms in the transferred peak ($90\hbar k$ total momentum kick) to the number of atoms in the peak that is left untransferred by the $\pi/2$-pulse. Spontaneous emission loss is the same for both peaks and therefore does not confound the measurement. We note that the two peaks have the same height, while the transferred peak has a narrower vertical width (for example, see Fig. 2). This indicates that the imperfect transfer efficiency arises from π-pulse velocity selectivity.

Spatial interference fringes. Owing to the long expansion time t_e, the launched atom cloud is effectively a point source, meaning that by the time of detection the vertical velocity distribution has been mapped onto the vertical position z through the relation $z \approx v_z t_e$ (v_z is the vertical velocity). The velocity dependent phase shift $nkv_z\delta T$ then leads to a position dependent phase shift[29] with corresponding wavelength $\lambda_z = 2\pi t_e/(nk|\delta T - \delta T_0|)$. Here δT_0 accounts for any velocity-dependent phase shifts from force gradients[29]. To observe the fringes, we reduce the fluorescence imaging time to 2.5 ms (see Fig. 5). We choose $\delta T = -50$ μs so that a full wavelength is visible on the atom cloud. For $\delta T = 100$ μs the smaller fringe period is completely blurred out by imaging heating of the atom cloud. The direct spatial interference contrast for $\delta T = -50$ μs is lower than the contrast with $\delta T = 0$ reported in Fig. 4b due to this blurring.

We use principal component analysis (PCA) to extract spatial fringes from a set of 20 interferometer runs. In addition to the fringe pattern, PCA is sensitive to shot-to-shot variation of the centre of mass position of the cloud. To minimize crosstalk between these effects, we correct for the vertical and horizontal motion before performing PCA. We find the position of the cloud centre of mass for each shot using Gaussian fits and then shift each image appropriately to remove the motion. The data are also smoothed with a 400 μm Gaussian filter before PCA. We identify the first principal component as the shape of the overall cloud envelope. Principal components two and three correspond to the cosine and sine components of the fringe pattern (Fig. 5).

Testing macroscopic extensions of quantum mechanics. In Extended Data Fig. 3, we show exclusion curves for the parameter space of a general class of minimal modifications to quantum mechanics[4]. The theory is characterized by two parameters: a critical length scale $\hbar/\sigma_q$ beyond which quantum superpositions decay (σ_q corresponds to the magnitude of spontaneous momentum kicks introduced by the modification), and a survival time τ_e that it takes for this decay to happen for an electron superposition larger than $\hbar/\sigma_q$. Therefore, different experiments can be referenced to an electron for comparison[4]. The critical length scale and survival time are free parameters of the theory that must be determined by experiment—there is no a priori assumption as to what their values should be[4].

To compare the bounds set by our experiment to the previous experimental status quo, we include exclusion curves for a number of other matter wave interference experiments that place bounds on this parameter space: atom interferometry with rubidium[25], caesium[37–39] and sodium[40]; neutron interferometry[41]; and interferometry with large molecules[42,43]. Molecular interferometry provides its strongest bounds on modifications to quantum mechanics of this form for submicrometre critical length scales, whereas the bounds from atom interferometry dominate at larger critical length scales due to the large wave packet separation.

We note that there are experiments demonstrating the preservation of entanglement over long distances, such as Bell experiments with photons[44] and the entanglement of many atomic spins[15]. While these experiments test quantum mechanics in a complementary way by generating entangled states, they do not create spatial superpositions of massive particles and thus do not bound the parameter space considered here.

Interferometer noise model and contrast estimation. Following ref. 11, we model the normalized population $P_1 \equiv N_1/(N_1+N_2)$ of an interferometer port as a random variable. P_1 is related to the phase Φ and contrast c of the interferometer by equation (1) above. We also assume that the interferometer noise X is normally distributed with PDF

$$f_X(x; w) = \frac{1}{w\sqrt{2\pi}} e^{-x^2/2w^2} \tag{2}$$

and that Φ and X are independent.

In the absence of noise ($w \to 0$), the PDF of P_1 is given by

$$g_{P_1}(p;c) = \frac{2}{\pi}\frac{1}{\sqrt{c^2-(2p-1)^2}}. \quad (3)$$

This function is supported on $\left(\frac{1}{2}-\frac{c}{2},\frac{1}{2}+\frac{c}{2}\right)$ and has asymptotes at the boundaries. Since Φ and X are independent, the PDF of P_1 for non-zero w can be computed by convolving $g_{P_1}(p;c)$ with $f_X(x;w)$:

$$f_{P_1}(p;c,w) = \int_{1/2-c/2}^{1/2+c/2} g_{P_1}(\tau;c) f_X(p-\tau;w)\mathrm{d}\tau \quad (4)$$

To experimentally determine w, we make the interferometer asymmetry δT large enough that $c \to 0$. In this case, P_1 is normally distributed, and the observed residual fluctuation in P_1 is used to estimate w. For the data reported in this work, we typically find $w \approx 0.03 \pm 0.005$. To estimate c, we use the maximum likelihood method[36] on a sequence of shots $\{p_1, \ldots, p_m\}$ at fixed δT. Specifically, we compute the likelihood

$$L(c;w,\{p_1,\ldots p_m\}) = \prod_{i=1}^{m} f_{P_1}(p_i;c,w) \quad (5)$$

taking the data points p_i and the measured value of w to be fixed parameters. The most likely value of c given the data is found by maximizing L as a function of c, or equivalently by solving

$$\frac{\partial}{\partial c}\ln L = 0 \Rightarrow \frac{\partial}{\partial c}\sum_{i=1}^{m}\ln f_{P_1}(p_i;c,w) = 0. \quad (6)$$

We maximize L numerically to generate the contrast estimates plotted in Fig. 4b.

The uncertainty in these contrast estimates arises from two sources. First, the standard error $\sigma_c(c)$ of the maximum likelihood method scales as the square root of the inverse of the Fisher information in the limit of a large number of samples m. The Fisher information $F(c)$ is defined by

$$F(c) = \int\left(\frac{\partial}{\partial c}\ln f_{P_1}(p;c,w)\right)^2 f_{P_1}(p;c,w)\mathrm{d}p \quad (7)$$

In the asymptotic limit $m \to \infty$, we have:

$$\sigma_c(c) = \frac{1}{\sqrt{m}}\frac{1}{\sqrt{F(c)}} \quad (8)$$

For $m \geq 20$, the error in the asymptotic approximation does not significantly contribute to the uncertainty. We verify this by computing the observed Fisher information F_o for each data set, where:

$$F_o(c;w,\{p_1,\ldots,p_m\}) = -\frac{1}{m}\frac{\partial^2}{\partial c^2}\sum_{i=1}^{m}\ln f_{P_1}(p_i;c,w) \quad (9)$$

Second, statistical uncertainty in the measurement of w propagates into uncertainty in the estimate of c. Both of these sources of uncertainty are reflected in the error bars shown in Fig. 4b.

Sample size. No statistical methods were used to predetermine sample size.

31. Kovachy, T. *et al.* Matter wave lensing to picokelvin temperatures. *Phys. Rev. Lett.* **114,** 143004 (2015).
32. McGuirk, J. M., Snadden, M. J. & Kasevich, M. A. Large area light-pulse atom interferometry. *Phys. Rev. Lett.* **85,** 4498–4501 (2000).
33. Rosi, G., Sorrentino, F., Cacciapuoti, L., Prevedelli, M. & Tino, G. M. Precision measurement of the Newtonian gravitational constant using cold atoms. *Nature* **510,** 518–521 (2014).
34. Chiow, S.-W., Kovachy, T., Hogan, J. M. & Kasevich, M. A. Generation of 43 W of quasi-continuous 780 nm laser light via high-efficiency, single-pass frequency doubling in periodically poled lithium niobate crystals. *Opt. Lett.* **37,** 3861–3863 (2012).
35. Szigeti, S. S., Debs, J. E., Hope, J. J., Robins, N. P. & Close, J. D. Why momentum width matters for atom interferometry with Bragg pulses. *New J. Phys.* **14,** 023009 (2012).
36. Greene, W. H. *Econometric Analysis* (Pearson, 2012).
37. Peters, A., Chung, K. Y. & Chu, S. High-precision gravity measurements using atom interferometry. *Metrologia* **38,** 25–61 (2001).
38. Chung, K.-Y., Chiow, S.-w., Herrmann, S., Chu, S. & Müller, H. Atom interferometry tests of local Lorentz invariance in gravity and electrodynamics. *Phys. Rev. D* **80,** 016002 (2009).
39. Lan, S.-Y., Kuan, P.-C., Estey, B., Haslinger, P. & Müller, H. Influence of the Coriolis force in atom interferometry. *Phys. Rev. Lett.* **108,** 090402 (2012).
40. Kasevich, M. & Chu, S. Measurement of the gravitational acceleration of an atom with a light-pulse atom interferometer. *Appl. Phys. B* **54,** 321–332 (1992).
41. Zawisky, M., Baron, M., Loidl, R. & Rauch, H. Testing the world's largest monolithic perfect crystal neutron interferometer. *Nucl. Instrum. Meth. A* **481,** 406–413 (2002).
42. Brezger, B. *et al.* Matter-wave interferometer for large molecules. *Phys. Rev. Lett.* **88,** 100404 (2002).
43. Eibenberger, S., Gerlich, S., Arndt, M., Mayor, M. & Tüxen, J. Matter-wave interference of particles selected from a molecular library with masses exceeding 10,000 amu. *Phys. Chem. Chem. Phys.* **15,** 14696–14700 (2013).
44. Ma, X.-S. *et al.* Quantum teleportation over 143 kilometres using active feed-forward. *Nature* **489,** 269–273 (2012).

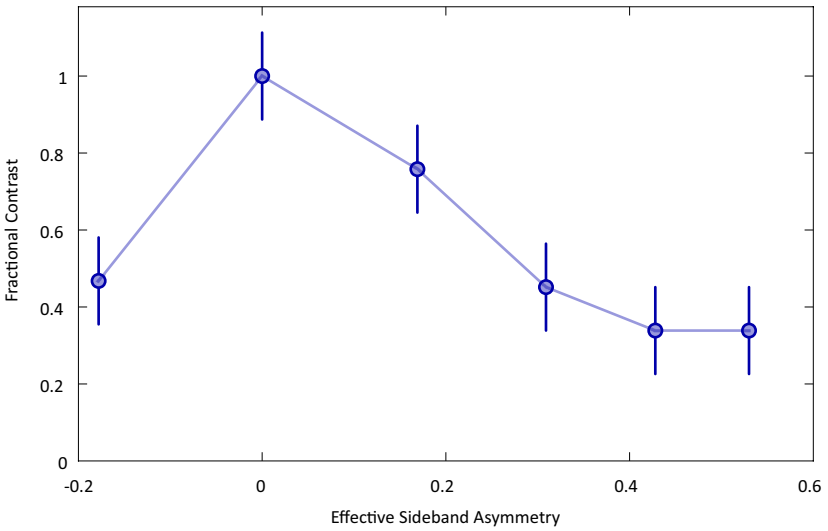

Extended Data Figure 1 | Dependence of contrast on absolute light shift compensation. For $30\hbar k$, the contrast as a fraction of its maximum value is plotted as a function of the asymmetry between the red and blue sidebands for one of the atom optics laser beams. To change the sideband asymmetry, we adjust the temperature of one of the frequency doubling crystals while keeping the sidebands of the second atom optics laser beam symmetric. Where P_{red} and P_{blue} are the respective optical powers in the red and blue sidebands, we define an asymmetry parameter $1-(P_{\mathrm{red}}/P_{\mathrm{blue}})$. Since the blue sideband is used to drive the Bragg transitions, we keep P_{blue} fixed in order to maintain constant Rabi frequency. This prevents us from reaching large negative values of the asymmetry parameter, because there is only enough total optical power available to increase P_{red} slightly without suppressing P_{blue}. In order to achieve a more negative effective value of the asymmetry parameter, we suppress the power in the carrier to half its usual amount for the one negative point in the plot. The carrier is blue detuned, so decreasing its power pulls the absolute light shift in the same direction as decreasing P_{blue}. To account for this, we plot the fractional contrast versus the effective asymmetry parameter that would yield the same light shift as the one that we implement, but at a fixed carrier power. The observed dependence of contrast on the sideband asymmetry indicates the importance of absolute light shift compensation for LMT interferometry. Error bars, 1σ.

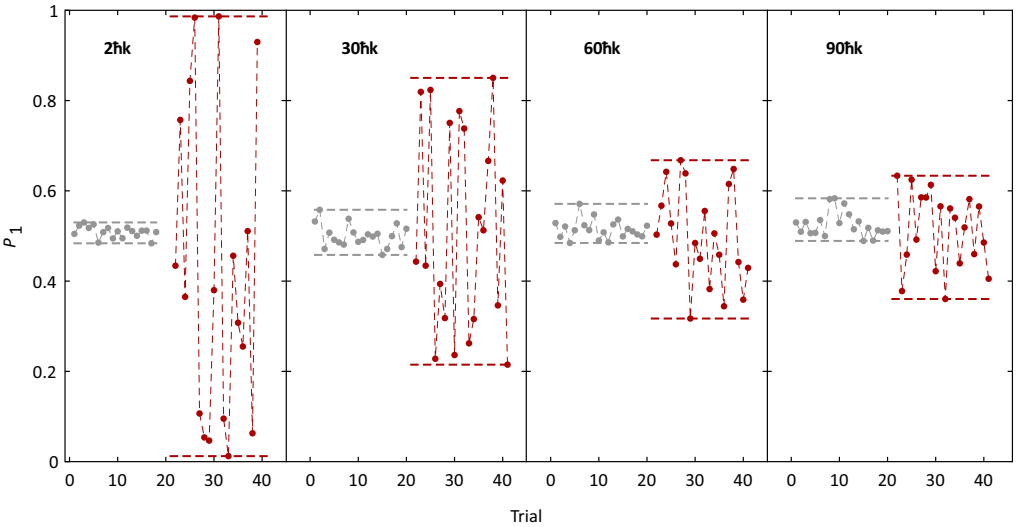

Extended Data Figure 2 | Examples of data showing interference contrast. Plots of P_1 versus experimental trial for $2\hbar k$, $30\hbar k$, $60\hbar k$ and $90\hbar k$. The red traces have small values of δT and therefore display interference contrast. As discussed in the main text, we do not observe a stable fringe because of the vibration of the retroreflection mirror. For comparison, the grey traces have large values of δT so that contrast is eliminated, and they therefore show the amount of background amplitude noise in P_1. Panels from left to right as follows. $2\hbar k$: red trace, $\delta T = 0\,\mu$s; grey trace, $\delta T = 2$ ms. $30\hbar k$: red trace, $\delta T = -15\,\mu$s; grey trace, $\delta T = 100\,\mu$s. $60\hbar k$: red trace, $\delta T = 0\,\mu$s; grey trace, $\delta T = 100\,\mu$s. $90\hbar k$: red trace, $\delta T = 1\,\mu$s; grey trace, $\delta T = -50\,\mu$s.

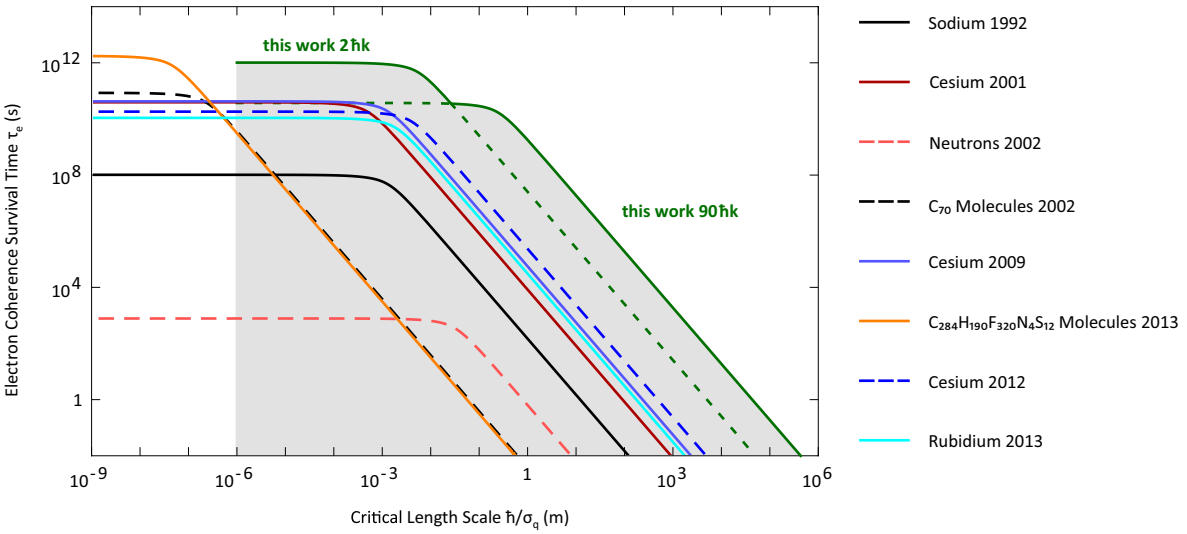

Extended Data Figure 3 | Bounds on macroscopic extensions of quantum mechanics. Exclusion curves for the minimal modification to quantum mechanics proposed in ref. 4. Points in this parameter space below a given curve in the plot have been ruled out by the corresponding experiment. The green curves show the bounds placed by the $2\hbar k$ and $90\hbar k$ atom interferometry results presented in this work. The grey, shaded area illustrates the region of parameter space excluded by these results. For sub-micrometre critical lengths, affected atoms would receive sufficiently large spontaneous momentum kicks to move out of the interferometer output ports. This results in atom loss and in a reduced sensitivity of the interference contrast to the decoherence rate. Therefore, we cut off the curves arising from our interferometry data at 1 μm. We also show exclusion curves from a sodium interferometer from 1992[40] (solid black), a caesium interferometer from 2001[37] (solid red), a neutron interferometer from 2002[41] (dashed red), a C_{70} molecular interferometer from 2002[42] (dashed black), a caesium interferometer from 2009[38] (solid blue), a caesium interferometer from 2012[39] (dashed blue), a $C_{284}H_{190}F_{320}N_4S_{12}$ molecular interferometer from 2013[43] (solid orange), and a rubidium interferometer from 2013[25] (solid cyan). For all of the exclusion curves, the change in slope occurs at a critical length scale value equal to the wave packet separation.

Extended Data Table 1 | Comparison with other matter-wave interference experiments

Description	Wave packet separation Δz (m)	Duration T (s)	Mass m (amu)	Acceleration sensitivity factor $m\Delta zT/\hbar$ $(m/s^2)^{-1}$
This work, Rb, 90 ħk	0.54	1.04	86.9	8×10^8
Cs, 2012	9×10^{-3}	0.25	132.9	5×10^6
Cs, 2009	3×10^{-3}	0.4	132.9	3×10^6
Rb, 2013	4×10^{-3}	0.35	86.9	2×10^6
Cs, 2001	1.1×10^{-3}	0.16	132.9	4×10^5
Na, 1992	3×10^{-3}	0.05	23	5×10^4
$C_{284}H_{190}F_{320}N_4S_{12}$, 2013	$\sim 3 \times 10^{-7}$	1.2×10^{-3}	$\sim 10^4$	60
Neutrons, 2002	0.07	4×10^{-5}	1.01	40
C_{70}, 2002	$\sim 10^{-6}$	1.9×10^{-3}	840	30

We compare the wave packet separation Δz, the duration T between the beam splitter and mirror sequences, and the mass m to those of a sodium interferometer from 1992[40], a caesium interferometer from 2001[37], a neutron interferometer from 2002[41], a C_{70} molecular interferometer from 2002[42], a caesium interferometer from 2009[38], a caesium interferometer from 2012[39], a $C_{284}H_{190}F_{320}N_4S_{12}$ molecular interferometer from 2013[43], and a rubidium interferometer from 2013[25]. Additionally, we compare the factor $m\Delta zT/\hbar$, which is directly related to the acceleration sensitivity (see the discussion of acceleration sensitivity in the main text). The wave-packet separation in our experiment is nearly an order of magnitude larger than the next largest value (from a neutron interferometer), and the duration in our experiment is more than four orders of magnitude longer than in the neutron interferometer with a nearly hundred times larger mass.